# Numerical assessment of surface roughness on a full scale propeller

(article starts on next page)

# Numerical assessment of surface roughness on a full scale propeller

**Rui Lopes[1], Arash Eslamdoost[1], Rikard Johansson[2], Seemontini RoyChoudhury[2], Rickard E. Bensow[1]**

[1]Department of Mechanics and Maritime Sciences, Chalmers University of Technology, Gothenburg, Sweden
[2]Kongsberg Hydrodynamic Research Centre, Kongsberg Maritime, Kristinehamn, Sweden

## ABSTRACT

This work addresses the performance of a full scale propeller in an open water setup for varying roughness heights, obtained with a RANS solver and the $k-\omega$ SST turbulence model. The application of roughness is done with wall functions and by resolving the boundary-layer. Two cases are considered for the same propeller geometry, one with and another without the anti-singing edge on the propeller blades. Baseline simulations without roughness are performed as well, and grid refinement studies are carried out to estimate the numerical uncertainty. The results showed that the influence of roughness is weak if wall functions are not used, whereas a significant decrease in thrust and torque is obtained if roughness is applied in conjunction with wall functions. The inclusion of the anti-singing edge leads to an increase in thrust and torque, but decrease in efficiency for low advance coefficients. The region of separated flow near the trailing edge of the propeller caused by the anti-singing edge is influenced by the roughness height, and is absent in the geometry without the anti-singing edge.

## Keywords

Marine Propeller, Turbulence Modelling, Roughness, Anti-singing Edge, Full Scale.

## 1 INTRODUCTION

The prediction of propeller performance is one of the key aspects in maritime engineering. To achieve this, both model testing and Computational Fluid Dynamics (CFD) may be considered. With the first approach, propeller characteristics at model scale operating in open water are directly obtained. However, it is impossible to guarantee Reynolds number similarity with a full scale operation. This results in a lower Reynolds number in the experiments, where transitional effects may play an important role (Baltazar et al 2018), and an appropriate scaling procedure is required to estimate the performance at full scale. On the other hand, CFD is capable of handling both model scale and full scale conditions. At model scale transitional effects are once again a challenge, as the usual "fully-turbulent" approach leads to negligible extents of laminar flow, and additional models are required to accurately predict transition and its triggering mechanisms such as natural or crossflow transition. Naturally, the inclusion of such

effects is important in order to enable fair comparisons with available experimental data where the flow was not tripped.

The much higher Reynolds number of the flow at full scale means that the fully turbulent approach can be considered as suitable, and so transition is not a concern. However, the flow is still strongly affected by the roughness of the blades and geometrical features. One of these features is the anti-singing edge - a chamfer of the trailing edge - used to prevent propeller singing, a noise causing phenomenon in which the vortex shedding at the trailing edge of the blade causes resonance on some frequencies of the blade (Carlton 1994).

The inclusion of surface roughness effects in CFD is a challenging topic which extends far beyond propeller performance (Eça et al 2022, Orych et al 2022). The resolution required to resolve the roughness on the surface leads to prohibitive computational requirements for practical applications and so its effects are usually accounted in a different fashion. If the boundary layer is fully resolved, i.e. if wall functions are not used, then roughness is included by a modification of the boundary conditions of the turbulence model on the surface. If wall functions are used, then a shift in velocity is computed and used to adjust the law of wall equation. Regardless of how the boundary layer is treated, the inclusion of roughness also requires some knowledge regarding its characterization, usually in the form of a value for the equivalent sand grain roughness (Andersson et al 2020). The determination of this value from measurements is not straightforward (Andersson et al 2020), and out of the scope of the present paper. Logically, if different approaches are chosen to represent the boundary layer, it is natural to expect that the application of roughness with the same value of equivalent sand grain roughness may have a different effect. In the context of propeller performance, the study of roughness is usually focused on its influence on cavitation (Asnaghi et al 2021, Sezen et al 2021).

This paper explores the effect of surface roughness on the propeller performance at full scale and on the flow field around the propeller blade, and the influence of how the boundary layer is handled. The effect of the anti-singing edge and its interaction with roughness is explored as well. To this end, simulations are performed for a controllable

pitch propeller at full scale in open water conditions. Two different variations of the geometry are considered, one with the anti-singing edge and one without it. The propeller performance is assessed for the two variants of the geometry and varying advance coefficients, and considering both a fully resolved boundary layer and wall functions, for a hydrodynamically smooth surface and for a rough surface with an equivalent sand-grain roughness of 30 μm. Variations of the roughness height for a constant advance coefficient are also considered.

The remainder of this paper is structured as follows: Section 2 presents the mathematical formulation of the problem and corresponding models used. The definition of the problem and numerical setup is described in Section 3. The main results of this work are presented and discussed in Section 4, while the main conclusions arising from the study are summarized in Section 5.

## 2 MATHEMATICAL FORMULATION

This paper addresses the flow of an incompressible, Newtonian fluid, governed by Reynolds-averaged Navier-Stokes (RANS) equations. The flow is assumed to be statistically steady, such that mean flow quantities are time averaged. Under these conditions, the continuity and RANS equations can be written as

$$\frac{\partial U_i}{\partial x_i} = 0, \tag{1}$$

$$\rho U_j \frac{\partial U_i}{\partial x_j} = -\frac{\partial P}{\partial x_i} + \frac{\partial}{\partial x_j}\left[\mu\left(\frac{\partial U_i}{\partial x_j} + \frac{\partial U_j}{\partial x_i}\right)\right] + \frac{\partial \tau_{ij}}{\partial x_j}, \tag{2}$$

where $U_i$ are the Cartesian components of the mean velocity vector, $x_i$ are the coordinates of the Cartesian coordinate system, $\rho$ is the density of the fluid, $P$ is the mean pressure of the fluid relative to the hydrostatic pressure, $\mu$ is the kinematic viscosity of the fluid and $\tau_{ij}$ is the Reynolds stress tensor.

The Reynolds stress tensor is determined based on the eddy-viscosity assumption, meaning that the Reynolds stresses are obtained from

$$\tau_{ij} = \mu_t \left(\frac{\partial U_i}{\partial x_j} + \frac{\partial U_j}{\partial x_i}\right) - \frac{2}{3}k\delta_{ij}, \tag{3}$$

where $\mu_t$ is the eddy-viscosity, $k$ is the turbulence kinetic energy and $\delta_{ij}$ is the Kronecker delta function.

The calculation of $k$ and $\mu_t$ is done through the use of the $k-\omega$ Shear Stress Transport (SST) model (Menter 1994). The $k-\omega$ model solves two transport equations, one for the $k$ and another for the specific turbulence dissipation rate $\omega$

$$\rho U_j \frac{\partial k}{\partial x_j} = P_k - D_k + \frac{\partial}{\partial x_j}\left[(\mu + \sigma_k \mu_t)\frac{\partial k}{\partial x_j}\right], \tag{4}$$

$$\rho U_j \frac{\partial \omega}{\partial x_j} = P_\omega - D_\omega + \frac{\partial}{\partial x_j}\left[(\mu + \sigma_\omega \mu_t)\frac{\partial \omega}{\partial x_j}\right]$$
$$+ 2(1 - F_1)\frac{\rho \sigma_{\omega 2}}{\omega}\frac{\partial k}{\partial x_j}\frac{\partial \omega}{\partial x_j}. \tag{5}$$

In these equations $P_k$, $D_k$, $P_\omega$ and $D_\omega$ are the production and dissipation terms of the turbulence kinetic energy and specific dissipation rate, respectively, whereas $\sigma_k$, $\sigma_\omega$ and $\sigma_{\omega 2}$ are constants and $F_1$ is a blending function.

It should be noted that the implementation of the SST model used in this work differs slightly from that given by Menter (1994). One of the differences lies in the calculation of the eddy-viscosity, which is determined from

$$\mu_t = \rho k \min\left(\frac{1}{\max\left(\omega, (SF_2)/0.31\right)}, \frac{0.6}{\sqrt{3}S}\right), \tag{6}$$

where $S$ is the mean strain rate magnitude and $F_2$ is a blending function of the model. This modification aims at preventing the growth of the eddy-viscosity in stagnation regions, as no limiter is used in $P_k$, unlike what is described by Menter (1994). The remainder of the formulation follows the original publication.

## 3 PROBLEM DEFINITION

All of the simulations performed for this work were done with the commercial CFD software STAR-CCM+ 2022.1.1. It employs the finite volume method for discretisation of the differential equations and the SIMPLE algorithm to solve the Navier-Stokes equations. The segregated flow solver is used to solve the system of linear equations and second order schemes are used for the discretisation of the convective term of all transport equations.

The computational domain is a cylinder with a diameter of $60D$ where $D$ is the diameter of the propeller. The domain is divided into two non-overlapping regions, an inner one consisting of a cylinder centered on the propeller, with a diameter of $1.25D$, and a length of $2D$, and the outer region that makes up the rest of the domain. In the inner region, the equations are solved in the body-fixed coordinate system, meaning that the flow can be considered as steady. The propeller is placed in the center of the domain, which has a length of $60D$, such that the inlet and outlet are placed $30D$ away from the propeller plane.

The velocity and turbulence quantities are specified at the inlet, whereas the pressure is specified at the outlet. A symmetry condition is enforced on the outer boundary of the domain. Two different approaches are used for the wall boundary conditions. In one case, the boundary layer is resolved and the shear-stress at the wall, $\tau_w$, is computed directly from its definition. In the second approach, wall functions are used instead.

The application of roughness depends on whether wall functions are used or not. If wall functions are not used, roughness is applied through the boundary condition for $\omega$, which is written as

$$\omega = \frac{\rho u_\tau^2}{\mu}S_r, \tag{7}$$

where

$$S_r = \begin{cases} \left(\frac{50}{k^+}\right)^2, & 5 \le k^+ \le 25 \\ \frac{100}{k^+}, & k^+ \ge 25. \end{cases} \tag{8}$$

$k^+$ is the dimensionless roughness height, determined as

$$k^+ = \frac{\rho u_\tau k_s}{\mu}, \qquad (9)$$

where $u_\tau = \sqrt{\tau_w/\rho}$ is the friction velocity and $k_s$ is the equivalent sand-grain roughness height.

If wall functions are used, then the log-law is given by

$$U^+ = \frac{1}{\kappa} \ln\left(y^+\right) + B - \Delta U^+, \qquad (10)$$

where $U^+$ and $y^+$ are the dimensionless velocity and wall coordinate, respectively, $\kappa$ is the von Kármán constant, $B$ is a constant and $\Delta U^+$ is the roughness function which represents the change in the velocity profile due to roughness. The roughness function of Demirel et al (2017) is used to compute $\Delta U^+$

$$\Delta U^+ = \begin{cases} 0, & k^+ \leq 3 \\ \frac{1}{\kappa} \ln\left(0.26 k^+\right)^{f(k^+)}, & 3 < k^+ \leq 15 \\ \frac{1}{\kappa} \ln\left(0.26 k^+\right), & 15 < k^+, \end{cases} \qquad (11)$$
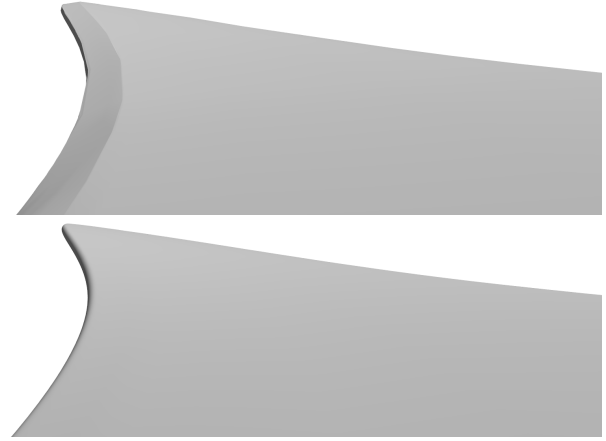
with

$$f(k^+) = \sin\left(\frac{\frac{\pi}{2}\log\left(\frac{k^+}{3}\right)}{\log(5)}\right). \qquad (12)$$

STAR-CCM+ uses a limiter by default to ensure that $k^+ \leq y^+$. For the purpose of this work, this limiter is disabled, otherwise it would be impossible to assess the influence of the different $k_s$ values, particularly when wall functions are not used.

Two propeller geometries are used, which differ only in the existence of the anti-singing edge. The trailing edge of a blade is depicted in Figure 1 for the two geometries. Several different conditions are simulated for each geometry. Nine advance coefficients ranging from $J = 0.34$ to $J = 0.992$ are considered, and the Reynolds number varies from $2.4 \times 10^7$ to $2.6 \times 10^7$. The advance coefficient is changed by only modifying the inlet velocity and keeping the rotation rate of the propeller constant, minimizing the change in Reynolds number. For the simulations with roughness, the equivalent sand-grain roughness is varied from 0.5 μm up to 300 μm. It is noted that while this is just a systematic variation to assess the change in the flow, the upper limit of this range might be excessive compared to what might be encountered for an actual propeller. The simulations for different advance coefficients are done for four different settings:

- Propeller geometry with the anti-singing edge with resolved boundary layer and smooth surface;

- Propeller geometry with the anti-singing edge with wall functions and smooth surface;

- Propeller geometry with the anti-singing edge with resolved boundary layer and rough surface ($k_s = 30$ μm);

- Propeller geometry without the anti-singing edge with resolved boundary layer and smooth surface.



Figure 1: Comparison of the two propeller geometries at the trailing edge with the anti-singing edge (top) and without the anti-singing edge (bottom).

The variation of $k_s$ is done for a single advance coefficient $J = 0.835$. These simulations are done for both propeller geometries, with and without wall functions.

In order to make the presentation of the data easier and to facilitate the discussion of the results, specific designations are used to identify the simulations. Calculations performed with wall functions are identified as WF, whereas simulations that resolve the boundary layer are instead labelled as WR. The simulations that account for roughness are usually identified by the corresponding roughness height value, or by the non dimensional height $k^+$ instead, while simulations that do not account for roughness are identified as "smooth". Finally, when addressing the influence of the anti-singing edge, simulations done on the geometry with this feature are referred to as "with ASE", whereas the calculations on the geometry without the anti-singing edge are mentioned as "no ASE".

Different cell types are used in the computational domain. The inner region around the propeller is filled with polyhedral cells, enabling the use of the advancing layer mesher for the prism layers, which generates high quality prism layers around the propeller blades and hub. The remainder of the domain is filled with hexahedral cells, which grow from the interface between the two regions to the outer boundaries of the domain. Figure 2 illustrates the grid topology around the propeller and on the propeller surface.

Two sets of five nearly geometrically similar grids are used for the simulations of all cases. One set is used for the simulations with wall functions and another set is used for the simulations where the boundary layer is resolved. In each set, the grids are designed to cover a grid refinement ratio of two, but due to the use of an unstructured grid topology the actual refinement is lower. Grids of the same refinement level between different sets have the same sizes and differ only on the number of prism layers and total thickness of the prism layer, to ensure suitability of the size of

the first cell above the wall for fully resolving the boundary layer in one set, and for the use of wall functions on the other. It should be mentioned that unlike what is commonly done with wall functions, the size of the first layer above the wall is not kept constant as the grid is refined. Instead, the coarsest grid is designed so that its $y^+$ is in the range of 100, meaning that the finest grid of the set is still suitable for the use of wall functions. Details of the grid sets used are given in Table 1 in terms of the number of faces on the propeller blades $\#S$ and total number of volume cells $\#V$ for the grid set where the boundary layer is resolved (WR) and for the grid set where wall functions are used (WF).
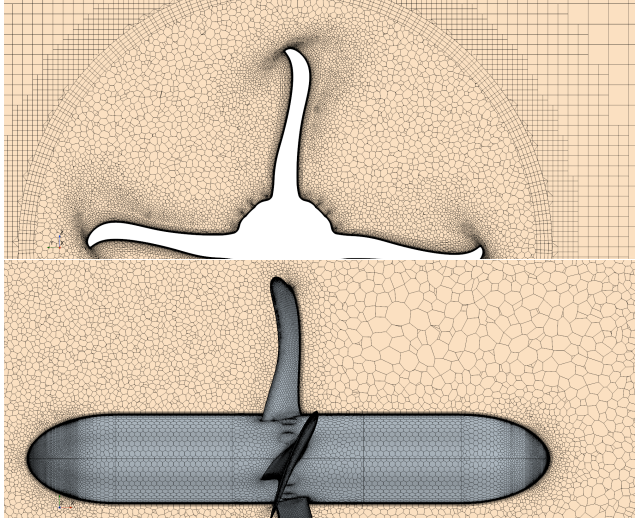


**Figure 2: Grid on the propeller plane (top) and around the propeller blades and hub (bottom).**

**Table 1: Details of the grids used for the propeller geometry with the anti-singing edge in terms of the number of faces on the propeller blades $\#S$ and total number of volume cells $\#V$ for the set where the boundary layer is resolved (WR) and for the set where wall functions are used (WF).**

| Grid | $\#S$ | $\#V$ (WR) | $\#V$ (WF) |
|------|-------|-----------|-----------|
| 5 | 78,200 | 7.8M | 5.1M |
| 4 | 106,140 | 14.3M | 9.5M |
| 3 | 145,853 | 23.7M | 15.8M |
| 2 | 194,036 | 36.6M | 24.4M |
| 1 | 234,426 | 52.3M | 35.2M |

The numerical error in steady simulations is typically divided into three different contributions (Roache 2009): discretization error, iterative error, and round-off error. The round-off error arises due to the finite precision of computers in representing and storing numbers. In this work, all the simulations are done in the double precision version of STAR-CCM+, making the round-off error negligible when compared to the remaining components.

The iterative error is caused by the iterative methods used to solve the linear system of equations. With regards to this error, the forces on the propeller blades and hub are monitored throughout the simulation, as well as the $L_2$ norm of the normalized residuals. The residuals are normalized such that they correspond to dimensionless variable changes in a simple Jacobi iteration. Although it is not possible to drive the residuals down to machine precision, when each simulation is stopped the $L_2$ norm of the residuals of all variables is around or lower than $10^{-5}$, and there is no significant change in the forces monitored. Thus, the iterative error is neglected as well.

This means that the dominant component of the numerical error is the discretization error, which is a consequence of the discretization of the governing equations and the computational domain. In order to estimate it, the procedure developed by Eça and Hoekstra (2014) is used. This procedure relies on a power series expansion of the error written as

$$e \approx \phi_i - \phi_0 = \alpha h_i^p, \qquad (13)$$

where $e$ is the discretization error, $\phi_i$ is the value of any given quantity of interest in grid $i$, $\phi_0$ is the estimate exact solution of mathematical model, $\alpha$ is an error constant, $p$ is the order of grid convergence and $h_i$ is the typical cell size. In Equation (13) there are 3 unknowns, $\alpha$, $p$, and $\phi_0$, meaning that one requires the solution on at least 3 grids to obtain the error. In the method of Eça and Hoekstra (2014), data from more than 3 grids is used, and Equation (13) is solved in the least-squares sense, in order to mitigate the effect of noise that is usually present in CFD calculations. Finally, the method estimates the numerical uncertainty of a given quantity at a desired grid based on the estimated discretization error, the variation of the solution between different grids, and the quality of the least-squares fit.

One important aspect in the application of methods based on grid refinement studies is the definition of the grid size. Generally, these methods require geometrically similar grids for their application, a constraint that is incompatible with the use of unstructured grids. The method is used nonetheless, with the typical cell size being defined based on the number of cell faces on the propeller blades such that $h_i = \left(\frac{1}{\#S}\right)^{1/2}$, as according to Rocha et al (2017).

The main quantities of interest addressed in this work are those that relate to the performance of the propeller, namely the thrust coefficient $K_T$, the torque coefficient $K_Q$, and the efficiency $\eta$. These are defined as

$$K_T = \frac{T}{\rho n^2 D^4}, \qquad (14)$$

$$K_Q = \frac{Q}{\rho n^2 D^5}, \qquad (15)$$

$$\eta = \frac{J K_T}{2\pi K_Q}. \qquad (16)$$

In these equations, $T$ and $Q$ are the propeller thrust and torque, respectively, whereas $n$ is the propeller rotation rate in rps. The skin-friction coefficient $C_f$ on the surface of the blades is presented as well, and it is written as

$$C_f = \frac{\tau_w}{\frac{1}{2}\rho U_{Ref}^2}, \qquad (17)$$

where $U_{Ref}$ is the reference velocity, computed as the velocity at 70% of the propeller radius, meaning that $U_{Ref} = \sqrt{V_A^2 + (0.7D\pi n)^2}$.

## 4 RESULTS

Figure 3 presents the relative variation for $K_T$, $K_Q$ and $\eta$, where the reference value considered corresponds to those obtained for the simulation with the resolved boundary layer and no roughness. Figure 3 shows that the application of roughness leads to a reduction of less than 1% in $K_T$ and $K_Q$ for the lowest advance coefficients, with a slight decrease in efficiency as well. As $J$ increases, $K_T$ and $K_Q$ decrease further, with the reduction in the former being stronger, which also leads to an overall decrease of the efficiency that reaches 4% at the highest advance coefficient simulated. When wall functions are used, a reduction in the thrust coefficient is observed, which is similar to that obtained if roughness is used. On the other hand, there is a stronger decrease on the torque coefficient, ultimately leading to a higher efficiency. This trend remains for most of the advance coefficients simulated with the exception of the highest one. For these conditions, the decrease of the propeller thrust is more pronounced than the decrease in torque, causing a very slight reduction in the efficiency, lower than 1%.
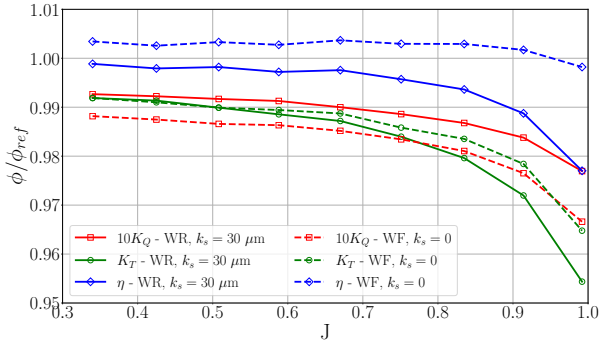


**Figure 3: Comparison of the performance of the smooth WF and rough WR ($k_s = 30$ μm) approaches relative to the smooth WR solution at varying advance coefficients for the geometry with the anti-singing edge.**

Tables 2 and 3 present the estimate of the numerical uncertainty obtained for the thrust and torque coefficients of the propeller for different advance coefficients and the smooth WR and WF approaches, as well as the WR approach with $k_s = 30$ μm. A general trend for both quantities is the increase of the uncertainty with the increase of $J$. Since the uncertainty is provided in relative terms, it must be mentioned that in some cases, particularly at the lowest advance coefficients, the estimated absolute value of the uncertainty is actually lower, but since $K_T$ and $K_Q$ decrease, this causes an increase in the relative uncertainty. Another trend in the data is that the highest uncertainty is typically obtained when the boundary layer is resolved and roughness is not applied, with the exception of the highest advance coefficient tested. In this regard, it is clearly seen that the use of wall functions leads to a much lower un-

certainty than the remaining approaches. Furthermore, the uncertainty of the different modelling approaches is considerably larger than the relative variation exhibited in Figure 3.

**Table 2: Estimate of the numerical uncertainty of the thrust coefficient obtained for several advance coefficients for the smooth WR and WF cases and the WR approach with a roughness height of $k_s = 30$ μm.**

|  | $U(K_T)$ | | |
|---|---|---|---|
| $J$ | WR $k_s = 0$ | WR $k_s = 30$ μm | WF $k_s = 0$ |
| 0.34 | 6.4% | 4.2% | 0.6% |
| 0.425 | 4.7% | 3.4% | 1.9% |
| 0.508 | 6.3% | 3.5% | 1.3% |
| 0.588 | 4.7% | 2.6% | 1.3% |
| 0.670 | 6.0% | 3.6% | 1.7% |
| 0.751 | 8.2% | 5.3% | 3.3% |
| 0.835 | 10.7% | 6.7% | 3.6% |
| 0.914 | 15.5% | 5.1% | 6.4% |
| 0.992 | 6.6% | 12.2% | 8.8% |

**Table 3: Estimate of the numerical uncertainty of the torque coefficient obtained for several advance coefficients for the smooth WR and WF cases and the WR approach with a roughness height of $k_s = 30$ μm.**

|  | $U(K_Q)$ | | |
|---|---|---|---|
| $J$ | WR $k_s = 0$ | WR $k_s = 30$ μm | WF $k_s = 0$ |
| 0.34 | 5.7% | 3.3% | 1.6% |
| 0.425 | 6.0% | 3.6% | 1.4% |
| 0.508 | 5.2% | 3.6% | 1.8% |
| 0.588 | 5.6% | 3.8% | 2.1% |
| 0.670 | 6.1% | 4.4% | 2.1% |
| 0.751 | 7.7% | 5.9% | 3.0% |
| 0.835 | 9.6% | 7.3% | 4.0% |
| 0.914 | 13.1% | 9.8% | 5.8% |
| 0.992 | 19.4% | 15.6% | 10.7% |

We now turn our attention to the variation of the roughness height for a single advance coefficient. Figure 4 shows the relative variation in efficiency and thrust and torque coefficients obtained at $J = 0.835$ as a function of the dimensionless roughness height for the simulations done with the resolved boundary layer and using wall functions. In this case, the values are given relative to the corresponding simulations without roughness.

Addressing first the simulations where the boundary layer is resolved, the application of roughness leads to a decrease in all quantities less than 1% for $k^+ < 1$. In the range $1 < k^+ < 10$ a significant reduction is observed in all quantities, with the thrust decreasing by almost 2%. As the roughness height is further increased up to $k^+ = 100$, only a small decrease is observed in the propeller performance. A difference in trend is observed for the simulation with the highest roughness computed, as the torque coefficient increases, causing a drop in the efficiency of around 1%. Although not shown in Figure 4, the friction and pressure components of the thrust and torque were compared. In the

case of the thrust coefficient, the increase of the roughness height causes a decrease in both the friction and pressure components, with the variation in the friction component being one order of magnitude lower than the pressure contribution. Thus, the change in $K_T$ is dominated by the pressure contribution, explaining the decrease as the roughness height increases. In the case of the torque coefficient, the increase of $k$ leads to a reduction of the pressure component, while the friction one increases. For all roughness levels but the highest one, the dominant effect is that of the pressure, leading to the decrease of torque. In the range of the two highest roughness heights simulated, the effect of the friction contribution is larger than that of the pressure component, leading to the overall increase in torque.

Analysing now the simulations where wall functions are used, it is clear that the influence is much greater than if the boundary layer is resolved. The decrease of $K_Q$ reaches 9%, while that of $K_T$ has a maximum value of 17%, for the highest value of roughness height tested. It should also be mentioned that despite using the same values of $k_s$ for both sets of simulations, the resulting mean $k^+$ on the propeller blades shows some differences. A peculiar behaviour occurs in the range $10 < k^+ < 22$, which corresponds to $15$ μm $< k_s < 30$ μm, in which the torque and thrust increase with the increase of $k_s$. In this particular range, the pressure components of both torque and thrust increase from $k^+ = 10$ to $k^+ = 22$, although the general trend of the pressure components of torque and thrust is to decrease with increasing roughness. This is observed for all other variations of roughness.
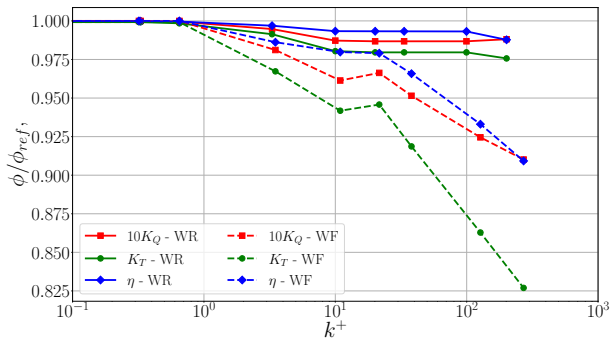


**Figure 4: Variation of $K_T$, $K_Q$ and $\eta$ with varying roughness height of the rough WR and WF conditions relative to the corresponding smooth conditions at $J = 0.835$ for the geometry with the anti-singing edge.**
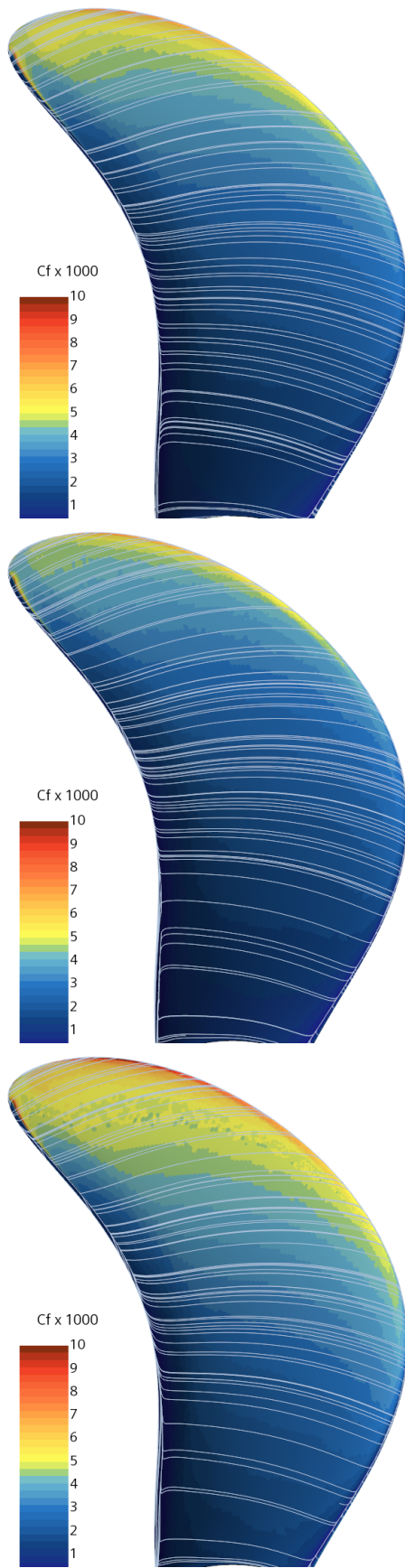
A comparison of the skin friction coefficient and limiting streamlines on the suction side of the blade at $J = 0.835$ is illustrated in Figure 5 for the WR and WF cases without roughness, and the WF solution with a roughness value of $k_s = 15$ μm. The solutions without roughness display a similar behaviour, with a small variation in $C_f$, most notably at the tip of the blade. Across all cases it is possible to see that the flow undergoes separation near the trailing edge, as a consequence of the anti-singing edge, although it does not extend until the tip of the blade. It is also noted that the geometrical influence of the anti-singing edge begins upstream of when flow separation takes place. The solution with wall functions and a roughness height of 15 μm exhibits the highest $C_f$, a natural consequence of the use of roughness. It was also found that roughness plays a role in the extent of the separation zone at the trailing edge if wall functions are used.

This is confirmed in Figure 6, which shows $C_f$ and streamlines on the blade for the WF solutions for three levels of roughness height ranging from $k_s = 15$ μm to $k_s = 300$ μm. Besides the increase of $C_f$ with increasing roughness height, it is seen that the extent of the separation zone at the trailing edge is also slightly affected by roughness, extending more towards the tip of the blade as roughness increases. Although not shown in the paper, the same does not hold true if wall functions are not used. When the WR approach is employed, the increase in $C_f$ for the highest roughness height is much smaller, and there is a minimal effect on the separation zone at the trailing edge.

Figure 7 presents the results obtained for the smooth WR sets for the two geometries tested. Significantly lower $K_T$ and $K_Q$ are obtained for the geometry without the ASE, resulting in slightly higher efficiency for most of the $J$ range tested. However, when the propeller is lightly loaded, there is a significant drop in the efficiency. The numerical uncertainty, given in the form of the error bars, is also considerably lower for the geometry without the ASE, with the exception of some conditions that exhibited non-monotonic converge and thus led to a very conservative estimate of the numerical error.

A comparison of the effect of roughness for the geometry without the anti-singing edge is presented in Figure 8. The trends observed match those discussed for the geometry with the anti-singing edge, as the influence of the roughness height is much smaller when the WR approach is used, when compared to the application of wall functions. The sporadic increase of $K_T$ and $K_Q$ at certain roughness heights is also observed. Comparing the results with those in Figure 4 shows that the variation of $K_T$ and $K_Q$ with the roughness height seems to be lower for the geometry without the anti-singing edge. Considering the WF case, the thrust coefficient exhibits a reduction of around 6% at $k^+ = 10$ for the geometry with ASE, whereas the corresponding simulation for the geometry without the anti-singing edge only decreases by 4%. A similar behaviour is observed for the torque coefficient, albeit with a larger variation, particularly at the highest roughness heights. Although not shown here, the estimated numerical uncertainty is also the lowest when wall functions are used, and tends to decrease with the increase in roughness height.

**Figure 5: Skin-friction coefficient and limiting streamlines on the suction side of the propeller blade at $J = 0.835$ for the smooth WR (top), smooth WF (middle) and rough WF $k_s = 15$ μm (bottom) conditions for the geometry with the anti-singing edge.**
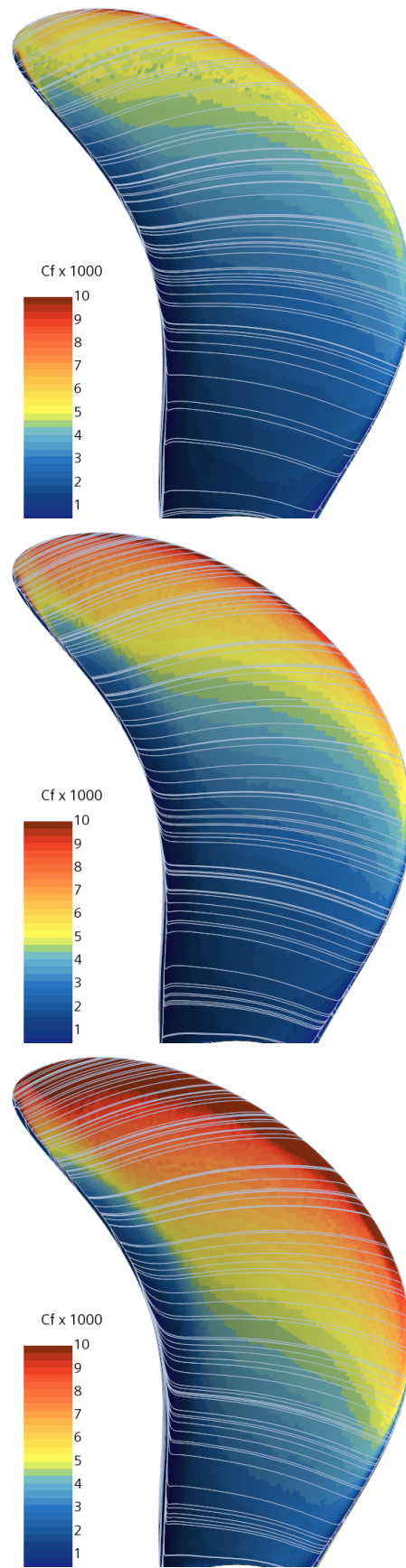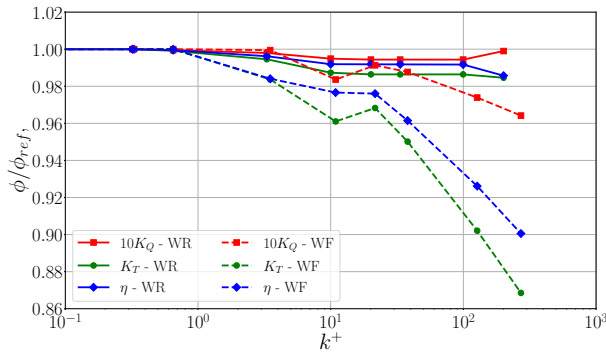
**Figure 6: Skin-friction coefficient and limiting streamlines on the suction side of the propeller blade at $J = 0.835$ for the rough WF conditions with $k_s = 15$ μm (top), $k_s = 50$ μm (middle) and $k_s = 300$ μm (bottom) for the geometry with the anti-singing edge.**
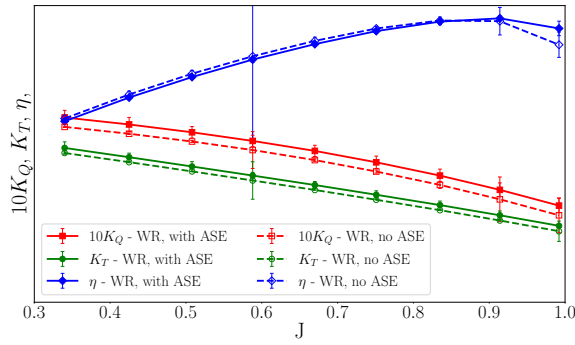
**Figure 7: Open water diagram for smooth WR conditions for the geometries with and without the ASE.**



**Figure 8: Variation of $K_T$, $K_Q$ and $\eta$ with varying roughness height of the rough WR and WF conditions relative to the corresponding smooth conditions at $J = 0.835$ for the geometry without the anti-singing edge.**

Figure 9 depicts the limiting streamlines and $C_f$ on the suction side of the propeller blade for different conditions. Similarly to the previous results, the increase in roughness height leads to an increase in $C_f$. However, in contrast to the geometry with the ASE, there is no separation near the trailing edge of the blade, even for the highest roughness height used with wall functions.

## 5 CONCLUSIONS

This study assessed the influence of roughness on the performance of a full scale propeller, considering its application through the use of wall functions and by resolving the boundary-layer and instead changing the boundary condition for $\omega$ at the wall. The importance of the anti-singing edge on the propeller blades was also investigated. A four blade controllable pitch propeller in an open water setup was simulated using the RANS equation and the $k-\omega$ SST turbulence model. Grid refinement studies were conducted for all cases in order to estimate the numerical uncertainty of the simulations. The main conclusions of the study are as follows:

- The use of wall functions for a propeller with a smooth surface, i.e. with no roughness applied, leads to a small reduction in the predicted thrust and torque coefficients. The difference grows larger with the increase of the advance coefficient, with the efficiency

of the propeller obtained with smooth wall functions being slightly higher than that of the smooth wall resolved approach, except at the highest $J$ considered.

- The application of roughness when the boundary layer is resolved leads to a small effect on the propeller performance, with a maximum decrease of 2.5% for the propeller thrust at the highest roughness height tested. On the other hand, the influence of roughness is stronger if wall functions are used, with the propeller thrust decreasing by over 15% for the highest roughness height tested.

- The comparison of the simulations performed with and without the anti-singing edge showed that this geometrical detail has a strong impact on the thrust and torque. The simulations performed without the anti-singing edge exhibited lower $K_T$ and $K_Q$, and an overall increase of efficiency. However, for conditions where the propeller is lightly loaded, the efficiency of the propeller is actually lower when the anti-singing edge is not present.

- The combined use of roughness and wall functions was seen to have an impact on the separated flow region obtained near the trailing edge of the propeller blades, as a consequence of the anti-singing edge. The influence of roughness is smaller for the geometry without the anti-singing edge, and no flow separation is visible near the trailing edge, regardless of the conditions.

The results of this study show that the effect of roughness depends greatly on whether wall functions are used or not. Even though resolving the boundary layer is the most accurate approach since it avoids the inherent limitations of wall functions, its combination with roughness is troublesome due to the requirements on the size of the first cell above the wall. This constraint means that in some situations the size of the near-wall cell might be lower than the roughness height, a physically questionable situation. On the other hand the use of wall functions allows for a much higher size of the first cell above the wall, thus avoiding this situation and also leading to reduced computational cost. Nonetheless, their application in the presence of strong adverse pressure gradients or separated flow should be avoided. When all factors are considered, wall functions seem to provide the best framework for the application of roughness, although it is clear that further development is required in this area. However, experimental data would be required in order to provide further confidence that the effects of roughness are better reproduced with wall functions rather than resolving the boundary layer.
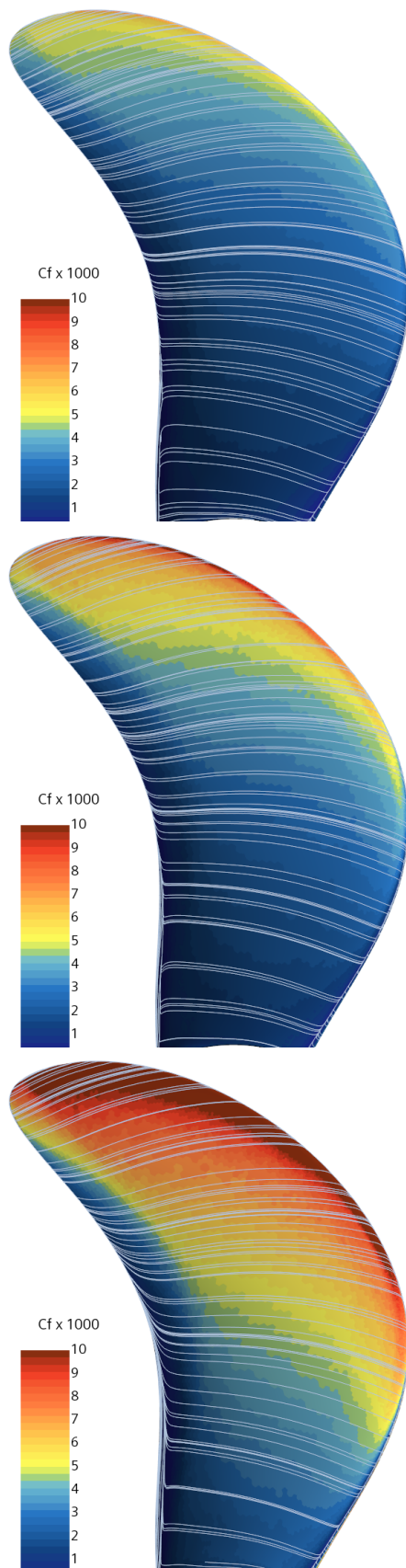
**Figure 9: Skin-friction coefficient and limiting streamlines on the suction side of the propeller blade at** $J = 0.835$ **for the smooth WR (top), rough WF** $k_s = 30\ \mu$**m (middle) and rough WF** $k_s = 300\ \mu$**m (bottom) conditions for the geometry without the anti-singing edge.**

## REFERENCES

Andersson, J., Oliveira, D. R., Yeginbayeva, I., Leer-Andersen, M. & Bensow, R. E. (2020). 'Review and comparison of methods to model ship hull roughness'. Applied Ocean Research **99**, 102119.

Asnaghi, A., Svennberg, U., Gustafsson, R. & Bensow, R. E. (2021). 'Propeller tip vortex mitigation by roughness application'. Applied Ocean Research **106**, 102449.

Baltazar, J., Rijpkema, D. & Falcão de Campos, J. A. C. (2018). 'On the use of the $\gamma - \tilde{R}e_{\theta_t}$ transition model for the prediction of the propeller performance at model-scale'. Ocean Engineering **170**, pp. 6–19.

Carlton, J. (1994). Marine Propellers and Propulsion. 4th ed. Elsevier.

Demirel, Y. K., Turan, O. & Incecik, A. (2017). 'Predicting the effect of biofouling on ship resistance using CFD'. Applied Ocean Research **62**, pp. 100–118.

Eça, L., Starke, A. R., Kerkvliet, M. & Raven, H. C. (2022). 'On the contribution of roughness effects to the scaling of ship resistance'. Journal of Ocean Engineering and Marine Energy **8**, pp. 539–551.

Eça, L. & Hoekstra, M. (2014). 'A Procedure for the Estimation of the Numerical Uncertainty of CFD Calculations Based on Grid Refinement Studies'. Journal of Computational Physics **262**, pp. 104–130.

Menter, F. R. (1994). 'Two-Equation Eddy-Viscosity Turbulence Models for Engineering Applications'. AIAA Journal **32**(8), pp. 1598–1605.

Orych, M., Werner, S. & Larsson, L. (2022). 'Roughness effect modelling for wall resolved RANS - Comparison of methods for marine hydrodynamics'. Ocean Engineering **266**, 112778.

Roache, P. J. (2009). Fundamentals of Verification and Validation. 2nd ed. Hermosa Publishers.

Rocha, A. L., Eça, L. & Vaz, G. (2017). 'On the Numerical Convergence Properties of the Calculation of the Flow Around the KVLCC2 Tanker in Unstructured Grids'. Proceedings of the VII International Conference on Computational Methods in Marine Engineering, Nantes, France.

Sezen, S., Uzun, D., Turan, O. & Atlar, M. (2021). 'Influence of roughness on propeller performance with a view to mitigating tip vortex cavitation'. Ocean Engineering **239**, 109703.